Spatial nonuniformity in heat transport across hybrid material interfaces

Yansha Jin, Chen Shao, John Kieffer, Michael L. Falk, and Max Shtein

Phys. Rev. B **90**, 054306 — Published 25 August 2014

DOI: 10.1103/PhysRevB.90.054306

Spatial Non-uniformity and Heat Transport Across Hybrid Material Interfaces

Yansha Jin[1,2], Chen Shao[2], John Kieffer[2], Michael L. Falk[1] and Max Shtein[2]

[1]*Materials Science and Engineering, Johns Hopkins University, Baltimore, Maryland 21218 USA*

[2]*Materials Science and Engineering, University of Michigan, Ann Arbor, Michigan 48109 USA*

Abstract

Successful thermal management in nanostructured devices relies on control of interfacial thermal transport. Recent measurements have revealed poor thermal transport across interfaces between two dissimilar materials, e.g. organic semiconductors and metals. In such systems, the interfacial thermal conductance, G_b , is dominated by the strength of interfacial bonding, but existing analytical models still fail to accurately predict G_b , especially for organic-metal interfaces. Growing interest in this research area calls for comprehensive understandings of interfacial thermal transport across hybrid material interfaces. Here we demonstrate that spatial non-uniformity has to be assessed in the calculation of G_b for interfaces with partial coverage or incommensurate growth that is characteristic of these interfaces. The interface between copper phthalocyanine (CuPc) and F.C.C metals (Ag, Al, Au) exhibits a six-fold difference between the metal's (~ 4 Å) and organic molecule's (~ 25 Å) lattice constant. Molecular dynamics simulations reveal the spatial variation of G_b, and a model is developed that considers the spatial variations in phonon transmission, successfully predicting G_b for many organic-metal interfaces.

I. INTRODUCTION

Strong interest in organic materials persists due to their wide range of applications in nanostructured devices, including lighting[1-3], displays[4-6], transistor-based logic[7-9], radio frequency identification[10,11], solar electricity generation[12,13] and, most recently, thermoelectric energy conversion[14-16]. The performance of these devices is often related to and limited by the thermal transport within the nanostructures and across dissimilar interfaces (e.g. between the active layers and electrodes, electrodes and packaging, *etc.*) common to these structures[17-19]. The ability to predict interfacial heat transport based on constituent material properties is therefore valuable, yet remains impossible in many important cases.

Interfacial thermal conductance, G_b , can be quantified as $G_b=q_{int}/\Delta T$, where q_{int} is the heat flux across the interface and ΔT stands for the interfacial temperature drop[20-23]. Advanced experimental techniques enable accurate measurements of G_b[24-26]. Figure 1 shows many of the experimentally measured G_b values[27-35], categorized by the type of interface; the three broad categories of interface are inorganic semiconductor-metal, organic materials-metal and organic-organic. The measured G_b values span two orders of magnitude, with the largest variation observed for metal-organic interfaces. The deciding factors for G_b depend on the material system and interfacial structure. In semiconductors with low doping concentrations heat flux is carried by phonons; hence, interfacial heat transport in all three categories in Figure 1 is dominated by phonon transmission. G_b based on phonon transmission is mostly affected by the mismatch between the intrinsic thermal properties (acoustic impedance, phonon density of states); however, for highly mismatched interfaces that also exhibit weak adhesion, G_b is most sensitive to the adhesion strength.[27,28,33] This dependence on interfacial bonding strength is the reason for the wide spread of G_b values in the mid-section of Figure 1, which represents weakly bonded,

dissimilar material interfaces: organic-metal. However, despite the experimental evidence for the correlation between G_b and adhesion strength at organic-metal interfaces, analytical models develped considering this correlation still fail to accurately predict the value of G_b.

We present an approach that improves existing capabilities of predicting interfacial heat transport at dissimilar interfaces by introducing factors that accounts for the spatial non-uniformity in phonon transmission. In Section II, a brief summary of the current theoretical models is presented, followed by discussion on the importance to include spatial non-uniformity factor (Section III), with supporting results from molecular dynamics (MD) simulation. Section IV presents the final form of the analytical model developed in this work. All findings are summarized in Section V.

II. THEORETICAL BACKGROUND

The general analytical form for G_b derived from the Boltzmann transport equation is[36-39]:

$$G_b = \frac{1}{4}\int_0^{\omega_{c-1}} \hbar\omega\tau^{1\to2} D_1(\omega)\frac{\partial f}{\partial T} v_{ph-1} d\omega \tag{1}$$

where ω is the phonon frequency which has a maximum cut-off at $\omega_{c\text{-}1}$, $D_1(\omega)$ is the phonon density of states of material 1, f_0 is Bose-Einstein distribution for phonons and $v_{ph\text{-}1}$ stands for the phonon velocity of material 1. $\tau^{1\to2}$ is the phonon transmission coefficient from material 1 to 2, which is the key parameter that varies in different models. In the acoustic mismatch model (AMM), $\tau^{1\to2}$ is frequency independent and relates to acoustic impedances; in the diffuse mismatch model (DMM), $\tau^{1\to2}$ is frequency dependent and determined by the phonon density of states overlap at the interface.

However, in case of G_b at organic-metal interfaces, the values predicted by the models discussed above do not match the measured ones. To account for interfacial bonding strength,

Prasher[40] introduced a harmonic spring with spring constant K_{int} into the AMM model. This approach improves the predictions somewhat. Table 1 shows the measured and calculated G_b of interfaces formed by small-molecule organic semiconductor (copper phthalocyanine (CuPc) or fullerene (C_{60}) or Sub-phthalocyanine (SubPc)) and common electrode metal materials (Ag, Al, Au). The parameters used in these calculations are shown in Table 2. Clearly, error still exists and is larger for some material combinations than for others; and our results in the following sections suggest the discrepancies are due to the neglect of spatially non-uniform bonding at the interface.

III. SPATIALLY NON-UNIFORM PHONON TRANSMISSION

Spatially non-uniform phonon transmission has been overlooked previously in part because phonons are a collective motion of atoms, and one might expect that variations in interfacial coverage at the nanometer scale should not affect the behavior of phonons whose wavelength is ~100 nm in common inorganic semiconductors. However, this might not be the case for organic materials. Here we develop a molecular dynamics (MD) approach that elucidates the spatial non-uniformity of phonon transmission across the interfaces of interest and show why this effect should be considered in theoretical predictions of G_b.

A CuPc-metal interface is presented in Figure 2, with atom coordinates obtained from a relaxed structure generated by MD simulations. To accomplish this, an accurate force field for CuPc was built and used to generate systems *in silico*[41] consisting of CuPc molecules deposited onto (111) surface of an FCC metal (Al, Ag, Au) lattice. At the interface, in the first monolayer, the planar CuPc molecules lay flat on top of the metal atoms. As clearly shown in Figure 2(b), the interfacial coverage from the first layer of the molecules is imperfect. The spacing between

two CuPc molecules can be as large as 2.5 nm, comparable to the phonon wavelength (~ 2 nm) of CuPc, and also sufficient to fit one or more metal atoms not "in contact" with a CuPc molecule.

The adsorption of CuPc molecules and other phthalocyanine molecules on FCC metals (111) substrates had studied extensively.[42,43,44] It is believed that when growing more than one monolayer (ML) of CuPc molecules, the surface interactions and intermolecular interactions together will force the first-layer organic molecules away from their initially energetically favorable positions. The total energy balance is considered in our MD simulations and the structure in Figure 2 is a result of this simulation, revealing substantial inhomogeneities in surface coverage and non-uniform bonding strengths across the interfacial plane. These non-uniformities are confirmed by experiment,[42,43,44] and give rise to spatial variation of thermal conductance.

Firstly, we confirm the non-uniformity of bonding strengths by evaluating the spatial distribution of effective spring constants (oriented perpendicular to the interface) of the atoms in the first layer of CuPc. The cross-plane effective spring constants of each atom are sampled by their kinetic energy and cross-plane displacements:

$$E_k = \frac{1}{2} K_{sp} \Delta z^2 \tag{2}$$

where E_k is the kinetic energy of each atom, Δz is the cross-plane displacement of the corresponding atom, and the resulting spring constant K_{sp} is also a per-atom property. The histogram of K_{sp} of the atoms in first layer of CuPc is shown in Figure 3. The H atoms are weakly bonded in the cross-plane direction, while Cu and N have stronger spring constants in this direction. The inset of Figure 3 shows one of these CuPc molecules scaled vertically by their

effective spring constants to better highlight the spatial non-uniformity of bonding strength. The center of the molecule bonds to the metal 5 times more strongly than the side atoms.

Consider now the other side of the interface: the metal. These interfacial metal atoms are divided into two environments, categorized by whether they are fully underneath a CuPc molecule from the first ML, or in the projected interstices of the first ML (see Figure 2-a). Figure 4 depicts these two regions as the "Pack" (Blue) and "Void" (Red) regions. Numerically, the "Pack" region is defined by several virtual cylinders centered at the copper atoms of CuPc; the radii of the cylinders are 6.58 Å, which is the distance from Cu to the furthest N atom in the CuPc molecule. This radius is chosen because the values of K_{sp} of the H atoms are significantly lower than the rest of the atoms in the first layer of CuPc, such that the metal atoms underneath could be more attracted to the second layer of CuPc.

An obvious shift in K_{sp} peaks for "Pack" and "Void" is observed in Figure 5 (a similar analysis for CuPc-Al is shown in the Supplemental Material[45]). The silver atoms without CuPc coverage ("Void") experience lower K_{sp} compared to those in the "Pack" region. The K_{sp} histogram for the silver atoms further away from the interface is plotted as "Bulk" in Figure 5: the interactions among silver atoms themselves are much stronger than the interfacial bonding strength.

The phonon density of states of these atoms is also presented Figure 5, calculated by velocity auto-correlation obtained by MD simulations. The 5 THz longitudinal peak is no longer observable for the interfacial atoms; and the 3 THz in the bulk vibrational spectrum is red shifted for both "Pack" and "Void", with the "Void" shifting 0.6 THz more. This red shift indicates that the weak interfacial spring constant can filter out the high-frequency modes.

MD simulation results also suggest that the thermal conductance differs between "Pack" and "Void" in the cross-plane direction. To extract the thermal conductance in the cross-plane direction, the heat auto-correlation function (HACF) of the interfacial silver atoms in "Pack" and "Void" regions is also calculated, following the Green-Kubo formalism. Due to the narrow sample volume in the cross-plane direction, the effective local thermal conductivities are obtained by the spectral analysis of the HACF:

$$k(\omega) = \frac{V}{3k_b T^2}\int_0^\infty \langle J(t)\cdot J(0)\rangle e^{-i\omega t}dt$$

$$= \frac{V}{3k_b T^2}\int_0^\infty \langle J(0)\cdot J(0)\rangle e^{-t/\tau_d} e^{-i\omega t}dt$$

$$= \frac{V\langle |J(0)|^2\rangle}{3k_b T^2(i\omega + 1/\tau_d)}$$

$$|k(\omega)| = \frac{k(0)}{\sqrt{1+(\omega\tau_d)^2}} \quad (3)$$

where V is the simulation volume, J is the heat flux and τ_d is the HACF decay time. The frequency-dependent thermal conductivity was calculated, and is shown in **Figure 6**. The thermal conductivity that is commonly measured and calculated corresponds to the value of $k(\omega)$ at the zero-frequency limit ($\omega \to 0$), which can be extrapolated following Eq. (3). The cut-off frequency in Figure 6 is 2 THz, matching the lowest observable peak in phonon density of states, assuring this cut-off is larger than the minimum allowed frequency in our small simulation volume. The effective thermal conductivity of the "Pack" region (0.56 W/mK) is larger than that of the "Void" (0.41 W/mK).

The above results regarding bonding strength and thermal conductance variations confirm the existence of spatial non-uniformity of phonon transmission at the interface, and suggest this

is the origin of the mismatch between previous models and measurements. From this point on, we focus on developing a more accurate analytical method for calculating G_b that accounts for the spatial non-uniformity.

IV THERMAL BOUNDARY CONDUCTANCE MODELING WITH SPATIAL NON-UNIFORMITY FACTORS

The transmission coefficient $\tau^{1\to2}$ is a function of bond strength and a correlation to the spatial non-uniformity. Simple averaging interfacial bonding over the interfacial area returns incorrect predictions of the overall phonon transmission, motivating a more careful analysis how a particular bonding distribution transmits phonons.

The interfacial bonding is often represented by the average spring constant $K_0=\langle K_{sp}\rangle$, which could be calculated from a measurable quantity: adhesion strength. However, the dependence of phonon transmission $\tau^{1\to2}$ on interfacial spring constant K_{int} is not linear, with the spring often behaving as a low pass filter in phonon transmission. Assuming $K_{int} = K_0$ in a calculation will yield the wrong transmission coefficient, because the averaging operation, $\langle K_{sp}\rangle$, and transmission coefficient calculation, $\tau^{1\to2}()$, are not commutable if the dependence is not linear:

$$\tau^{1\to2}(\langle K_{sp}\rangle) \neq \langle \tau^{1\to2}(K_{sp})\rangle \tag{4}$$

This inequality is essentially due to the spatial distribution of the spring constants that affect the phonon transmission locally. A correction related to this commutation error is needed.

Our correction and modifications are based on a previous model,[39] and consider diffuse and inelastic scattering. Previous work has shown that diffuse scattering is a more valid assumption for "rough" interfaces (roughness more than one atomic layer) at room temperature, and often the contribution from the inelastic channel is non-negligible. At weakly bonded

interfaces (e.g. CuPc-metal), the contribution from inelastic scattering becomes even larger[45]. Thus, we use the inelastic limit of the transmission coefficient in diffuse scattering:

$$\tau_0^{1\to 2} = \frac{J_2}{J_1 + J_2} \quad , \quad J_i = \int_0^{\omega_{c-i}} \hbar\omega D_i(\omega) f_0 v_{ph-i} d\omega \tag{5}$$

where τ_0 is the phonon transmission coefficient under the inelastic limit. Additionally, it is believed that the interfacial bonding strength behaves like a low-pass filter[28,33,40] which weighs the frequency independent phonon transmission coefficient: $\tau^{1\to 2}$= W $\tau_0{}^{1\to 2}$, where W is the weighing factor. As a low-pass filter, below the dominant phonon frequency ω_0, W(K_{int})=1; beyond ω_0, W is assumed to have the Lorentzian form:

$$W(K_{\text{int}}) = \frac{1}{\sqrt{1 + (\omega_0 / \omega_i - 1)^2}}, \quad \omega_0 > \omega_i . \tag{6}$$

The ratio $\omega_0 / \omega_i = (\sqrt{(K_1 K_2)} / K_{\text{int}})^{0.5}$, according to the general relation between spring constant and frequency $\omega \propto \sqrt{K}$. Thus, the total transmission coefficient $\tau^{1\to 2}$ =W(K_{int}) $\tau_0^{1\to 2}$ is not a linear function of K_{int}, and the commutation inequality expressed by Eq. (4) applies: we cannot use K_0 directly.

The simplest way to implement the correction is to replace the average spring constant K_0 by an effective value K_b that accounts for the differences caused by the commutation. If the weighing factor follows Eq. (6), the highest order the spring constant in the equation is $K_{sp}{}^{-1}$. Thus, we can assume the effective value K_b using:

$$K_b^{-1} = \frac{1}{N} \sum_{i=1}^{N} K_{i-sp}^{-1} \tag{7}$$

The ratio R_c=K_b/K_0 will come into the model as a correction term $\tau^{1\to 2}$=W($R_c K_0$) $\tau_0^{1\to 2}$. As discussed above, the correction exists due to the non-uniform distribution of K_{sp}, which should

be a function of the interfacial coverage percentage, x_c%. In the case of CuPc-metal interfaces investigated above, the x_c% is the percentage of the area of "Pack" to the total area of the interface. When the area of the "Pack" region grows, the two peaks in the K_{sp} histogram (**Figure 5**) tend to merge into one; if the "Pack" region shrinks, the more isolated organic molecule islands will result in the peaks pushing each other further away.

Performing MD simulations for every combination of materials and interface structure is impractical at the present. It would be more useful instead to have a model independent of the MD simulations. To accomplish this, we would like to reproduce the $\{K_{sp}\}$ distributions with statistically generated data sets, then calculate the general dependence of the ratio, $R_c=K_b/K_0$, on x_c%. The generated $\{K_{sp}\}$ contains two normal distributions $\{k_p\}$(pack) and $\{k_v\}$(void). The peak positions K_P and K_V are separated by a value of dk, with distribution variance $d\omega$ (see inset of **Figure 7**), defined as follows:

$$K_0 = K_P x_c\% + K_V(1 - x_c\%) \tag{8}$$

The average spring constant K_0 is fixed at the measured value, and the peak positions K_P and K_V vary with x_c%. The separation dk decreases monotonically with x_c%, and the distribution variance $d\omega$ should be minimized (x_c=100% and x_c=0%), which are written as,

$$dk = K_0(1 - x_c\%) \ , \qquad d\omega = K_0(1 - x_c\%)x_c\% \tag{9}$$

For each coverage percentage x_c%, 100 data sets for $\{K_{sp}\}$ are generated, and the effective spring constant K_b is then calculated following Eq. (7). In **Figure 7**, K_b/K_0 ratio is plotted against x_c%. The $R_c(x_c\%)$ is validated by MD simulations for a CuPc/FCC metal interface; the coverage x_c% is 50.4% and the plot (Figure 7) returns K_b/K_0=0.787. K_b is also calculated using MD-calculated $\{K_{sp}\}$ for all the interfacial atoms by Eq. (2) yields K_b/K_0=0.77, a close match.

Using $R_c(x_c\%)$ ~0.77 in the final expression of our model is:

$$G_b = \frac{1}{2} W(K_0 R_c(x_c\%)) \tau_0^{1\to 2} \int_0^{\omega_{c1}} \hbar\omega D(\omega) \frac{\partial f_0}{\partial T} v_{ph,1} d\omega \quad (10)$$

where the dependence of G_b on the spring constant is calculated for all three CuPc/FCC metal interfaces and plotted in Figure 8, with validated input constants shown Table 2.

The calculations are in close agreement with MD simulations[28]. The values lie within error-bars of each data point. The model is not only accurate, but also easy to adapt to different material systems. This can be accomplished by obtaining the two extra input parameters directly from simple measurements: the average spring constant K_0 can be obtained from adhesion tests, and the coverage percentage x_c% can be estimated using crystallographic data for the materials involved.

For example, we calculate G_b values for C_{60}/Ag and SubPc/Ag and compare them to the experimental values shown in Table 3 and Table 1. By using the measured K_0 in Table 1, parameters in Table 2 and the crystal structures documented in other references[45,46], an accurate G_b value is obtained by Eq. (10).

V. SUMMARY

This work reports the spatially non-uniform phonon transmission for organic semiconductor and metal interfaces. However, we believe that non-uniformity may be an important consideration in many more systems, at least for those in which partial interfacial coverage is accompanied by a large spatial variation in effective interfacial spring constants. This effect of non-uniformity on heat transmission may have been overlooked in the past due to the difficulties in experimental measurements and molecular dynamics simulations for complex organic systems. Lastly, we would like to highlight the theoretical model developed here that considers the spatial variations.

It allows one to calculate interfacial thermal conductance accurately with the measured adhesion and documented lattice structures of the materials as input parameters. The reduction in interfacial thermal conductance caused by spatial non-uniformity is most significant around 50% interfacial coverage. Thus, aside from the adjusting the interfacial heat transfer *via* chemical bonding, further tuning of heat transfer across hybrid material interfaces can be realized by engineering the atom/molecule packing at the interface. We expect this development may lead to a clearer understanding of interfacial heat transfer and assist design and performance evaluations in practical applications.

ACKNOWLEDGEMENTS

Y.J., C.S., J.K., M.S. thank the Center of Solar and Thermal Energy Conversion, an Energy Frontier Research Center funded by the U.S. Department of Energy, Office of Science, Office of Basic Energy Sciences under Award No, DE-SC0000957. Y.J. and M.L.F. acknowledge support of the National Science Foundation under Grant No. DMR-1005398.

REFERENCES

[1] B. W. D'Andrade, and S. R. Forrest, White Organic Light-Emitting Devices for Solid-State Lighting. *Adv. Mater.* **16**, 1585-1595 (2004).

[2]Y. Cui, Y. Yue, G. Qian and B. Chen Luminescent functional metal-organic frameworks. *Chem. Rev.* **112**, 1126-1162 (2011).

[3]Y. Sun, N. C. Giebink, H. Kanno, B. Ma, M. E. Thompson and S. R. Forrest, Management of singlet and triplet excitons for efficient white organic light-emitting devices. *Nature* **440**, 908-912 (2006).

[4]T. Sekitani, H. Nakajima, H. Maeda, T. Fukushima, T. Aida, K. Hata and T. Someya Stretchable active-matrix organic light-emitting diode display using printable elastic conductors. *Nature Mater.* **8**, 494-499 (2009).

[5]A. Nathan, A. Kumar, K. Sakariya. P. Servati, S. Sambandan and D. Striakhilev Amorphous silicon thin film transistor circuit integration for organic LED displays on glass and plastic, *IEEE J. Solid-State Circuits* **39**, 1477-1486 (2004).

[6]G. H. Gelinck, H. Edzer, A. Huitema, E. van Veenendaal, E. Cantatore, L. Schrijnemakers, Jan B. P. H. van der Putten, T. C. T. Geuns, M. Beenhakkers, J. B. Giesbers, B-H Huisman, E. J. Meijer, E. M. Benito[1], F. J. Touwslager, A. W. Marsman, Bas J. E. van Rens and Dago M. de Leeuw Flexible active-matrix displays and shift registers based on solution-processed organic transistors. *Nature* **3**, 106-110 (2004).

[7]B. Crone, A. Dodabalapur, Y.-Y. Lin, R. W. Filas, Z. Bao, A. LaDuca, R. Sarpeshkar, H. E. Katz and W. Li Large-scale complementary integrated circuits based on organic transistors. *Nature* **403**, 521-523 (2000).

[8]M. Hamedi, R. Forchheimer and O. Inganas, Towards woven logic from organic electronic fibres. *Nature Mater.* **6**, 357-362 (2007).

[9]C.W. Tseng and Y. T. Tao, Electric bistability in pentacene film-based transistor embedding gold nanoparticles. *J. Am. Chem. Soc.* **131**, 12441-12450 (2009).

[10]P. F. Baude, D. A. Ender, M. A. Haase, T. W. Kelley, D. V. Muyres and S. D. Theiss Pentacene-based radio-frequency identification circuitry. *Appl. Phys. Lett.* **82**, 3964 (2003).

[11]R. Rotzoll, S. Mohapatra, V. Olariu, R. Wenz, M. Grigas, K. Dimmler, O. Shchekin and A. Dodabalapur Radio frequency rectifiers based on organic thin-film transistor. *Appl. Phys. Lett.* **88**, 123502 (2006).

[12]P. Peumans, A. Yakimov and S. R. Forrest, Small molecule weight organic thin film photodetectors and solar cells. *J. Appl. Phys.* **93**, 3693 (2003).

[13]S. Günes, H. Neugebauer and N. S. Saricifitci, Conjugated polymer-based organic solar cells. *Chem. Rev.* **107**, 1324-1338 (2007).

[14]O.Bubnova, Z. U. Khan, A. Malti, S. Braun, M. Fahlman, M. Berggren and X. Crispin Optimization of the thermoelectric figure of merit in the conducting polymer poly(3,4-ethylenedioxythiophene), *Nature Mater.* **10**, 429-433 (2011).

[15]B. Zhang, J. Sun, H. E. Katz, F. Fang and R. L. Opila, Promising thermoelectric properties of commercial PEDOT:PSS materials and their Bi_2Te_3 powder composites. *ACS Appl. Mater. Interfaces* **11**, 3170-3178 (2010).

[16]Y. Jin, S. Nola, K. P. Pipe and M. Shtein, Improving thermoelectric efficiency in organic-metal nanocomposites via extra-low thermal boundary conductance. *J. Appl. Phys.* **114**, 194303 (2013).

[17]X. Qi and S. R. Forrest, Thermal analysis of high intensity organic light-emitting diodes based

on a transmission matrix approach. *J. Appl. Phys.* **110**, 124516 (2011).

[18]N. E. Coates, S. K. Shannon, B. McCulloch, K. C. See, A. Majumdar, R. A. Sgalman and J. J. Urban Effect of interfacial properties on polymer-nanocrystal thermoelectric transport. *Adv. Mater.* **25**, 1629-1633 (2013).

[19]B. H. Hamadani, D. A. Corley, J. W. Ciszek, J. M.Tour and D. Natelson, Controlling charge injection in organic field-effect transistors using self-assembled monolayers. *Nano Lett.* **6**, 1303-1306 (2006).

[20]P. L. Kapitza, *J. Phys., USSR* **4**, 181 (1941).

[21]G. L. Pollack, Kapitza Resistance. *Rev. Mod. Phys.* **41**, 48 (1969).

[22]R. E. Peterson and A. C. Anderson, The Kapitza thermal boundary resistance. *J. Low Temp. Phys.* **11**, 639-665 (1973).

[23]E. T. Swartz and R. O. Pohl, Thermal-boundary resistance. *Rev. Mod. Phys.* **61**, 605-668 (1989).

[24]D. G. Cahill, Thermal conductivity measurement from 30 to 750 K: the 3ω method. *Rev. Sci. Instrum.* **61**, 802-808 (1990).

[25]T. Borca-Tasciuc, A. R. Kumar and G. Chen, Data reduction in 3ω method for thin-film thermal conductivity determination. *Rev. Sci. Instrum.* **72**, 2139-2147 (2001).

[26]P. E. Hopkins, B. Kaehr, L. M/. Phinney, T. P. Koehler, A. M. Grillet, D. Dunphy. F. Garcia and C. J. Brinker, Measuring the thermal conductivity of porous transparent SiO_2 films with time domain thermoreflectance. *J. Heat Transfer* **133**, 061601 (2011).

[27]Y. Jin, A. Yadav, K. Sun, H. Sun, K. P. Pipe and M. Shtein Thermal boundary resistance of copper phthalocyanine-metal interface. *Appl. Phys. Letts.* **98**, 093305 (2011).

[28]Y. Jin, C. Shao, J. Kieffer, K. P. Pipe and M. Shtein, Origin of thermal boundary conductance of interfaces involving organic semiconductors. *J. Appl. Phys.* **112**, 093503 (2012).

[29]A. J. Schmidt, K. C. Collins, A. J. Minnich and G. Chen, Thermal conductance and phonon transmissivity of metal-graphite interfaces. *J. Appl. Phys.* **107**, 104907 (2010).

[30]R. J. Stevens, A. N. Smith and P. M. Norris, Measurement of thermal boundary conductance of a series of metal-dielectric interfaces by the transient thermoreflectance technique. *J. Heat Transfer* **127**, 315-322 (2005).

[31]A. M. Marconnet, N. Yamamoto, M. A. Panzer, B. L. Wardle and K. E. Goodson, Thermal conduction in aligned carbon nanotube-polymer nanocomposites with high packing density. *ACS Nano* **5**, 4818-4825 (2011).

[32]Q. Li, C. Liu and S. Fan, Thermal boundary resistance of carbon nanotubes in contact with metals and polymers. *Nano Letters* **9**, 3805-3809 (2009).

[33]M. D. Losego, M. E. Grady, N. R. Sotoos, D. G. Cahill and P. V. Braun, Effect of chemical bonding on heat transport across interfaces. *Nature Mater.* **11**, 502-506 (2012).

[34]P. E. Hopkins, L. M. Phinney, J. R. Serrano and T. E. Beechem, Effects of surface roughness and oxide layer on the thermal boundary conductance at aluminum/silicon interfaces. *Phy. Rev. B* **82**, 085307 (2010).

[35]P. E. Hopkins, P. M. Norris, R. J. Stevens, T. E. Beechem and S. Graham, Influence of interfacial mixing on thermal boundary conductance across a chromium/silicon interface. *J. Heat Transfer* **130**, 062402 (2008).

[36]P. Reddy, K. Castelino and A. Majumdar, Diffuse mismatch model of thermal boundary conductance using exact phonon dispersion. *Appl. Phys. Lett.* **87**, 211908 (2005).

[37]R. Prasher, T. Tong, A. Majumdar, An acoustic and dimensional mismatch model for thermal

boundary conductance between a vertical mesoscopic nanowire/nanotube and a bulk substrate. *J. Appl. Phys.* **102**, 104312 (2007).

[38]J. C. Duda, J. L. Smoyer, P. M. Norris and P. E. Hopkins, Extension of the diffuse mismatch model for thermal boundary conductance between isotropic and anisotropic materials. *Appl. Phys. Letts.* **95**, 031912 (2009).

[39]J. C. Duda, T. E. Beechem, J. L. Smoyer, P. M. Norris and P. E. Hopkins, Role of dispersion on phononic thermal boundary conductance. *J. Appl. Phys.* **108**, 073515 (2010).

[40]R. Prasher, Acoustic mismatch model for thermal contact resistance of van der Waals contacts. *Appl. Phys. Lett.* **94**, 041905 (2009).

[41]C. Shao, Y. Jin, K. P. Pipe, M. Shtein and J. Kieffer, Simulation of crystalline and amorphous copper phthalocyanine: force filed development and analysis of thermal transport mechanisms. *J. Phys. Chem. C* **118** 9861 (2014)

[42] I. Kröger, B. Stadtmüller, C. Stadler, J. Ziroff, M. Kochler, A. Stahl, F. Pollinger, T-L Lee, J. Zegenhagen, F. Reinert and C. Kumpf, Submonolayer growth of copper-phthalocyanine on Ag(111). *New Journal of Physics* **12** (2010) 083038

[43] C. Stadler, S. Hansen, I. Kröger, C. Kumpf and E. Umbach Tuning intermolecular interaction in long- range-ordered submonolayer organic films. *Nature Phys*. **5**, 153 (2009)

[44] B. Stadtmuler, I. Kröger, F. Reinert and C. Kumpf, Submonolayer growth of CuPc on noble metal surface. *Phys. Rev. B* **83**, 085416 (2011)

[45] See Supplemental Material at [URL] for molecular dynamic simulation results for CuPc-Al system; and inelastic contribution to thermal boundary conductance in CuPc-metal systems.

[46]N. Jiang, Y. Wang, Q. Liu. Y. Zhang, Z. Deng, K. H. Ernst and H. J. Gao Polymorphism and chiral expression in two dimensional subphthalocyanine crystals on Au(111). *Phys. Chem.*

Chem. Phys. **12**, 1318-1322 (2010).

[47]W. I. F. David, R. M. Ibberson, J. C. Matthewman, K. Prassides, T. J. S. Dennis, J. P. Hare. H. W. Kroto. R. Taylor and D. R. M. Walton, Crystal structure and bonding of ordered C_{60} . *Nature* **353**, 147-149 (1991).

Table 1 | Thermal boundary conductance for five organic-metal interfaces measured and calculated by various models. Calculation follows acoustic mismatch (AMM) and diffuse mismatch models(DMM) that documented in the references[36-39]. Prasher's model[37] considers the interfacial bonding strength and is calculated by implementing K_{sp} values shown in this table. Experiemental values(Exp) and MD calculated values are also presented.

Organic	***Metal***	****K_{sp} (N/m)***	***Exp. G_b (MW/m^2K)***	***AMM G_b (MW/m^2K)***	***DMM (Debye) G_b (MW/m^2K)***	***Prasher G_b (MW/m^2K)***	***MD G_b (MW/m^2K)***
CuPc	*Au*	1.4	19 ± 5	52	25	13	22
CuPc	*Ag*	1.0	13 ± 3	62	33	8	17
CuPc	*Al*	5.3	50 ± 15	286	62	156	52
C_{60}	*Ag*	1.1	16 ± 6	37	34	4	-
SubPc	*Ag*	1.1	14 ± 7	49	33	11	-

* calculated from previous publication and validated by peel-off tests, refer to reference 28

Table 2 | Parameters used for analytical models, including phonon velocity both transverse(TA) and longitudinal(LA), material density and phonon cut-off frequency that are used in all G_b calculation in this current work. The phonon velocities and cut-off frequencies are calculated by MD simulation[41] and ab-initio calculations.

Material	***V_{ph} (TA) (m/s)***	***V_{ph} (LA) (m/s)***	***Density (g/cm^3)***	***Cut-off Freq. (THz)***
CuPc	1130 *	-	1.63	4.7 *
Ag	2058 †	4003 †	10.5	5.7 †
Al	3625 †	6606 †	2.7	9.9 †
Au	1418 †	2113 †	19.5	5.3 †

† validated by Ab-initio calculations

* validated by MD simulations[41]

Table 3 | G_b calculated by the model (Jin G_b) reported in Section IV. The effective ratio K_b/K_0 is obtained from curve in Figure 7 by using the coverage percentage calculated from the crystal structure, except that of CuPc/Ag interface, which is obtained by MD simulations.

Organic	***Metal***	***Jin G_b (K_{inf}) (MW/m^2K)****	***x_c%***	***K_b/K_0***
CuPc	*Au*	20	50.4	0.787
CuPc	*Ag*	18	50.4	0.77 †
CuPc	*Al*	59	50.4	0.787
C_{60}	*Ag*	27	47.4	0.776
SubPc	*Ag*	18	40.1	0.782

† obtained from MD simulations * calculated by Eq. (10)

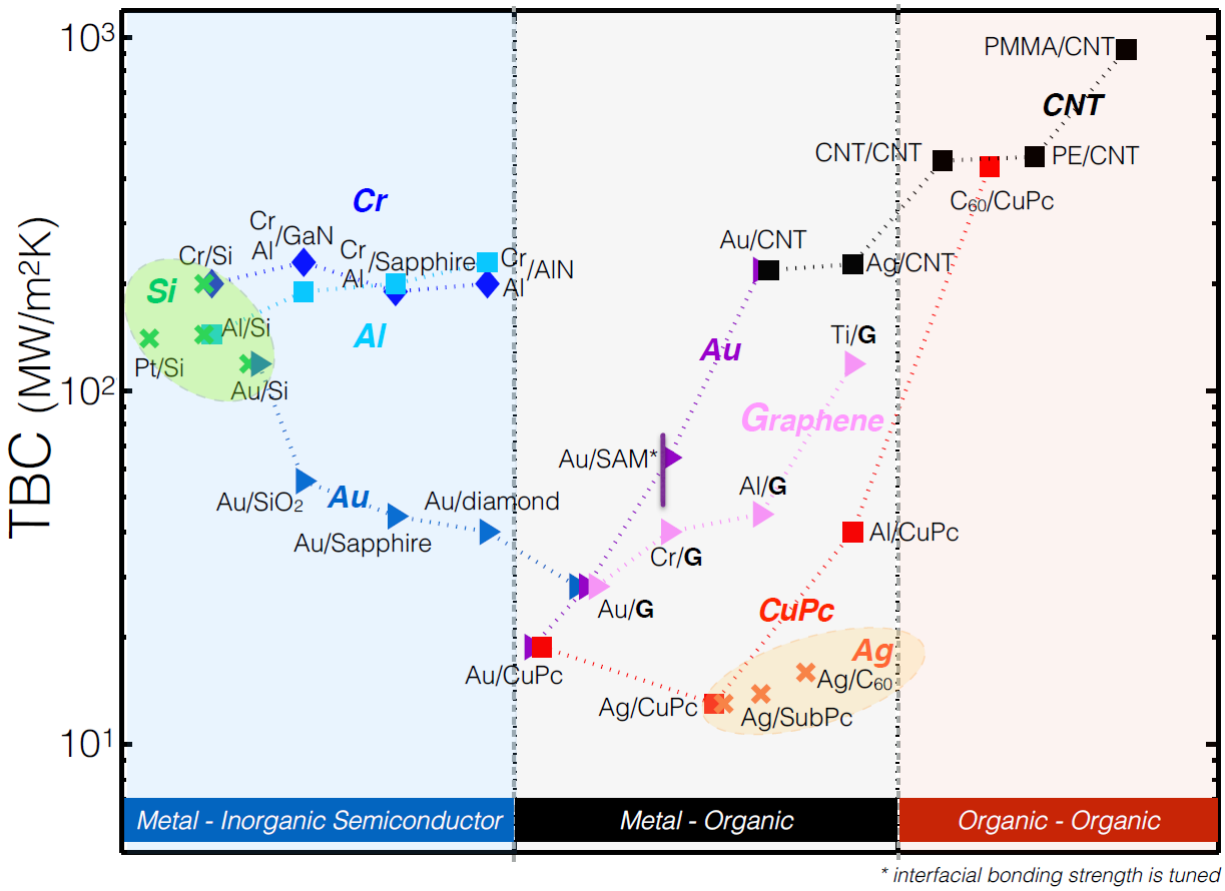

Figure 1 | Thermal boundary conductance for various interfaces. The measured values of thermal boundary conductance, $G_{b,}$ for various interfaces from multiple references. The interfaces are categorized into 3 groups: Left-(Blue) panel presents G_b of metal-inorganic semiconductor interfaces; Middle-(Grey) panel contains G_b data points of metal-organic interfaces; Right-(red) panel is for organic-organic interfaces. Data points with same marker type and color correspond to interfaces that share one material: this material is shown in bold font in the same color.

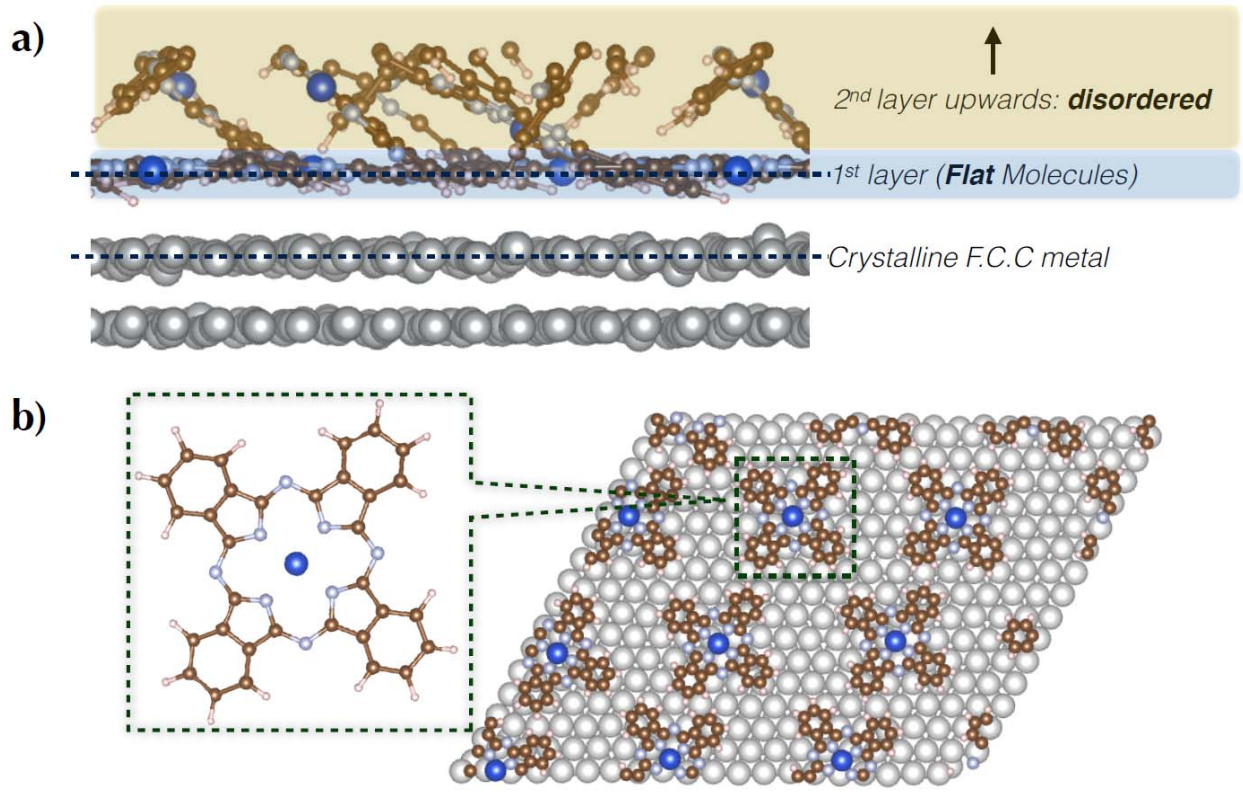

Figure 2 | Copper Phthalocyanine (CuPc)-F.C.C. metal (Ag, Al, Au) interface. Depiction of CuPc-F.C.C. metal interfaces: the atom coordinates are obtained from the relaxed structure of molecular dynamics simulation. a) Side view of the interface: the metal is in crystalline state; and CuPc molecules are disordered from the 2nd layer upwards while the first layer molecules lay flat. b) Top view of the interface alongside with structure of an enlarged CuPc molecule.

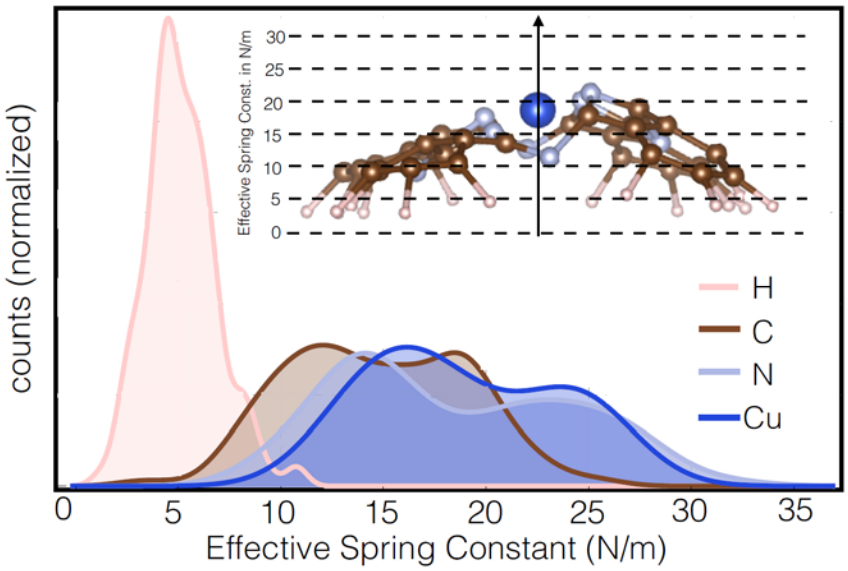

Figure 3 | Effective spring constants of atoms in the 1st layer CuPc. Effective spring constants, K_{sp} (cross-plane) are sampled using molecular dynamics simulations. The distribution of K_{sp} of each type of atoms (H, C, N, Cu) are presented as histograms: Cu and N atoms at the center of the molecule own larger spring constants compare to C and H atoms that are further from center. The inset is a side view of one particular CuPc molecule vertical spanned according to K_{sp}.

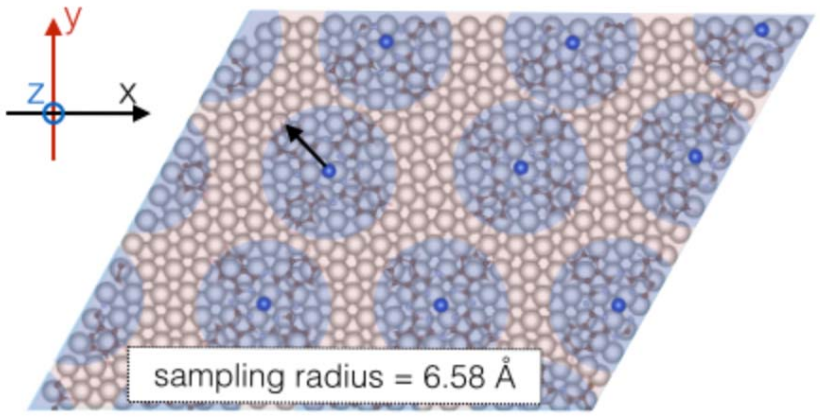

Figure 4 | "Pack" and "Void" environments of the first layer of metal atoms. The organic molecules have larger intermolecular spacings (>10 Å) than that of F.C.C. metal (~4 Å). The metal surface does not have full coverage by the organic molecules. If the metal atoms are topped by the CuPc molecules (within 6.58 Å radius, centered at the copper atoms), those are grouped in "Pack"-marked as blue; otherwise, the metal atoms belongs to the "Void" region.

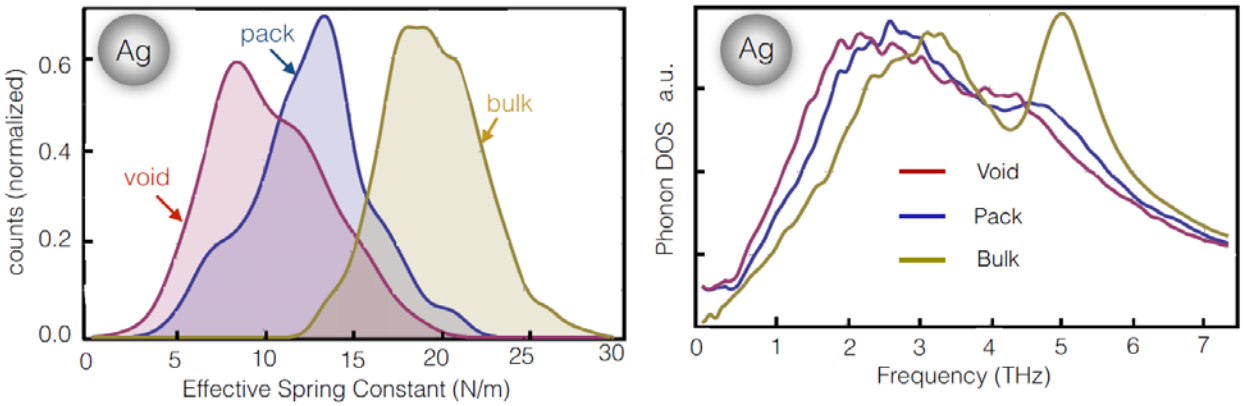

Figure 5 | Effective spring constants and phonon density of states of interfacial Ag atoms in "Pack", "Void" and in "Bulk". (Left) Histograms of effective spring constants (cross-plane). Peak value of K_{sp} in "Void" and "Pack" regions are separated by ~5 N/m, while both weaker in bonding compared to the "bulk" silver - sampled few layers underneath the interface. (Right) Phonon density of states (DOS) also show differences among the three groups: 5 THz (LA) peak cannot be observed at the interface; the phonon DOS of "Void" red shifted further compared to that of "Pack".

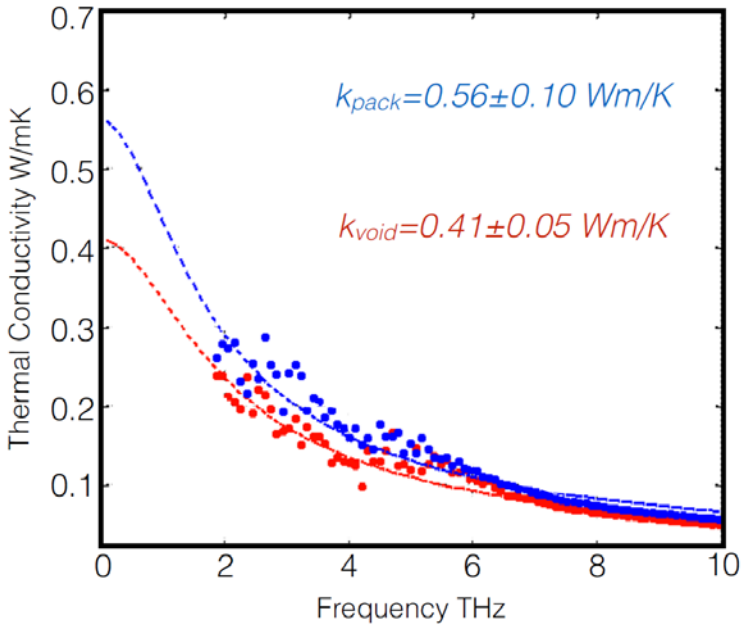

Figure 6 | Cross-plane interfacial thermal conductivity. Thermal conductivity in cross-plane direction (*z* axis in Fig. 4) calculated using Green-Kubo formalism. Size effect extrapolation is needed due to the narrow length sampled in cross-plane direction. $k(0)$ is fitted using Eq. (3) for both "Pack" and "Void" starting from 2 THz (the first peak value in Fig. 5) onwards, with thermal conductivity of the "Pack" 25% larger than that of the "Void".

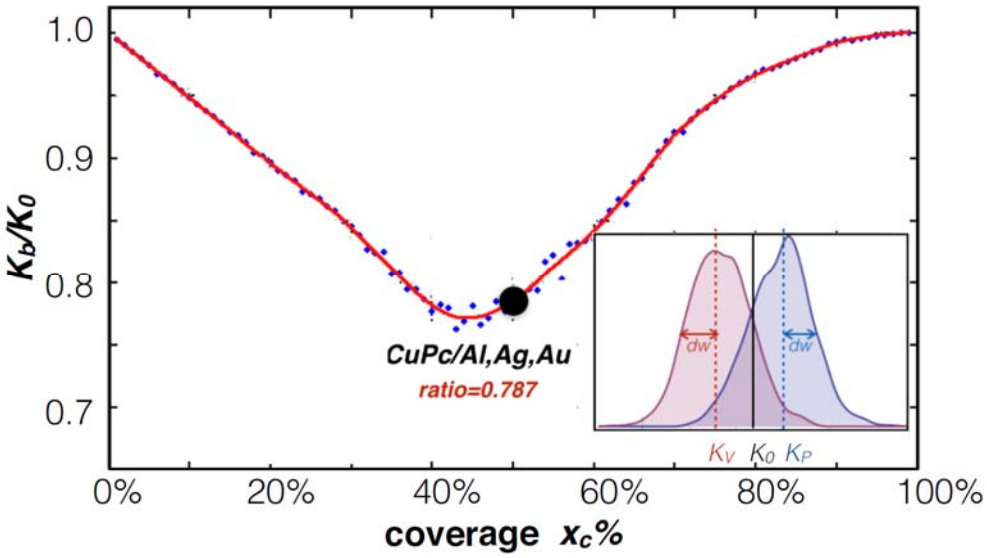

Figure 7| Effective Ratio K_b/K_0 versus the coverage percentage of the interface (x_c%). The ratio is a single parameter function of x_c%. The spring constant value that correctly calculates the boundary conductance is $K_b=1/\langle K^{-1}\rangle$ which differs from $K_0=\langle K\rangle$ by the factor of this effective ratio. An example distribution of $\{K_{sp}\}$ is presented in the inset. The ratio is 0.787 for CuPc-F.C.C. metal(Al, Ag, Au) interfaces.

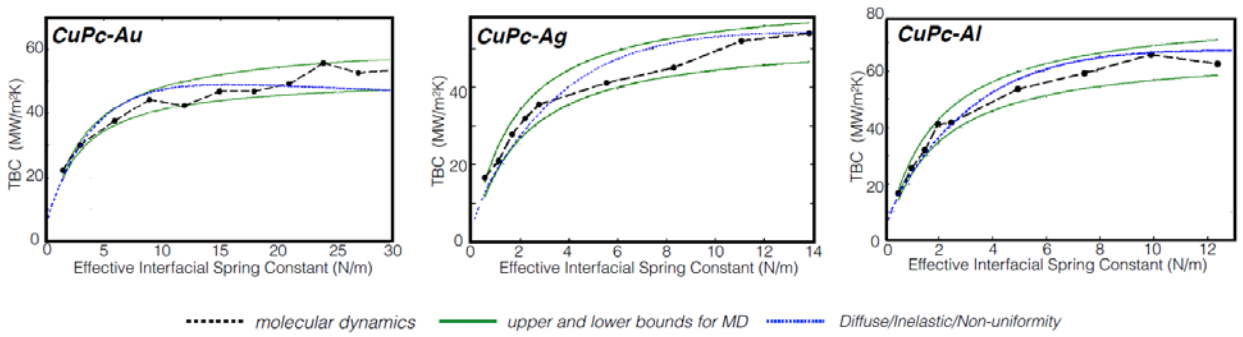

Figure 8 |Thermal boundary conductance of CuPc-F.C.C. metal interfaces versus K_{sp}. (Blue-dotted) Calculated by the model proposed here (Eq. (10)), considering diffuse and inelastic phonon scattering with partial interfacial coverage. (Black-dashed w/ black round markers) Molecular dynamics simulated G_b with upper and lower bounds draw separately in green lines.